HiSST: 2nd International Conference on High-Speed Vehicle Science Technology
11–15 September 2022, Bruges, Belgium

Stability of nozzle wall boundary layer in hypersonic facilities

Olivier Chazot[1], Geoffrey Andrews[2], Dániel G. Kovács[3], Guillaume Grossir[4]

Abstract

Hypersonic facilities are essential for the investigation of aerothermodynamic phenomena which have a direct impact on high-speed vehicles' design. The flow quality and characterization is of utmost importance for the ground testing experiment. The paper is looking at the expansion flow in a hypersonic nozzle and presents a methodology to determine the stability characteristics of the boundary layer developing along the nozzle wall. It offers the occasion to discuss and investigate how the turbulent boundary layers generated in a hypersonic nozzle. The selected test case is that of the accelerating flow within the axially contoured nozzle of the VKI Longshot facility. The design of its nozzle profile is first presented followed by the experimental characterization of its expansion flow inside the nozzle. The stability analysis of the nozzle wall boundary layer is finally exposed with a discussion on the physical mechanisms responsible for the development of instabilities.

Keywords: Hypersonic, boundary layer, stability, nozzle wall, Longshot

Nomenclature

Acronyms

RMS	Root Mean Square

Roman symbols

Cp	Specific heat at constant pressure (J/kg.K)
Cv	Specific heat at constant volumee (J/kg.K)
e	internal energy (J/kg)
f	frequency (Hz)
h	Static enthalpy (J/kg)
k	Roughness height (m)
P	Static pressure (Pa)
r	Radial nozzle coordinate (m)
Re	Reynolds number
s	Surface distance coordinate (m)
T	Static temperature (K)
x	axial nozzle coordinate (m)

Greek symbols

α	Complex streamwise wavenumber (1/m)
β	Spanwise wavenumber (1/m)
η	Self-similar wall-normal BL coordinate
μ	Dynamic viscosity (Pa.s)
ω	Angular frequency (1/s)
ρ	Density (kg/m^3)
ξ	Streamwise boundary layer coordinate

[1] *von Karman Institute for Fluid Dynamics, Waterloosesteenweg 72, B-1640, Sint-Genesius-Rode, Belgium, olivier.chazot@vki.ac.be*
[2] *Purdue University, 701 W. Stadium Ave. West Lafayette, IN 47907-2045, USA*, geoffreymgandrews@gmail.com
[3] *von Karman Institute for Fluid Dynamics / University of Liège, Waterloosesteenweg 72, B-1640, Sint-Genesius-Rode, Belgium / Allée de la Découverte 9, B-4000, Liège, Belgium, daniel.gabor.kovacs@vki.ac.be*
[4] *von Karman Institute for Fluid Dynamics, Waterloosesteenweg 72, B-1640, Sint-Genesius-Rode, Belgium, guillaume.grossir@vki.ac.be*

Copyright © 2022 by author(s)

Sub- and Superscripts

w	Wall conditions	e	Boundary layer edge
hyp	HYPNOZE conditions	k	Roughness height conditions
ref	reference state		

1. Introduction

The development of aerospace application requires an improved understanding of aerothermodynamic phenomena to master at best the design of hypersonic vehicles. Hypersonic transition is one of the main phenomena to occur in high speed regime and will have to be taken into account in all aerospace design. Such phenomenon starts with perturbations, that could come from the freestream or emanate from the vehicle's wall, which are reaching the boundary layer flow and generate different mode of oscillations. Those modes are propagating as waves which will grow, interact and become unstable. It will lead by several mechanisms to transition toward turbulent regime in the flow [1] [2].

The onset of hypersonic boundary layer transition has a dramatic impact on the wall heat transfer which imposes strong design constraints for the thermal protection system and directly affects the mass budget and the structural material concepts. The LTT also has direct consequences on the drag of the aerospace vehicle and its trajectory, on its stability and maneuverability, on the engine performance and its operation if one considers high speed propulsion. As shown in [3], pending on the configuration, there could be more than a 10-fold impact on the nominal laminar heat transfer and drag. All the structural parts of the vehicle have a direct influence on LTT phenomena, as isolated roughness, gaps, cavities, … but are also directly affected by a transitional boundary layer. All these constraints must be carefully considered during the design phase of the vehicle.

For doing so the design process resort largely on hypersonic facilities which also need to be understood from their domain of operation and the testing conditions they could provide. Those facilities are equipped with contoured nozzles to provide uniform hypersonic flows. They also present non negligeable boundary layers that develop along the nozzle wall which could disturb the freestream with the noise they eventually radiate. To study where those turbulent boundary layers appear in a hypersonic nozzle it is proposed to analyze their stability using the Linear Stability Theory (LST). We shall first present briefly how to define the profile of a contoured nozzle. It then will be reported about the measurements inside the hypersonic nozzle for the characterization of the boundary layer. Finally, the stability of the nozzle wall boundary layer will be studied with a first analysis using LST. Those investigations are done for the VKI Longshot facility for which the methodology is applied for the analysis of the nozzle wall boundary layer stability. It should help to provide some insight on the physics of the flow developing in a hypersonic nozzle.

2. Longshot nozzle design

The geometry of the VKI Longshot contoured nozzle is used hereafter. This short-duration gun tunnel is a reference European facility used to reproduce reentry flow conditions at both high Mach numbers and high Reynolds numbers [4] [5]. It relies on the compression of pure nitrogen up to large pressures and large temperatures before expanding it through an axisymmetric contoured nozzle. The large stagnation pressure and temperature involved (p_0=166MPa and T_0=2400K for the nozzle considered herein) induce significant deviations from a thermally and calorically perfect gas behavior, even though the flow total enthalpy remains moderate so that there is no chemistry taking place within the expansion. High-temperature and dense gas effects were both accounted for during the nozzle design process using a state-of-the-art equation of state for nitrogen [6] as implemented within the VKI in-house HYPNOZE design code [7]. HYPNOZE relies on the method of characteristics for the design of an inviscid nozzle contour. The latter being then corrected for viscous effects and the overall nozzle length being optimized to maximize the core flow dimensions. The resulting viscous contour of the Longshot contoured nozzle used hereafter is illustrated in Fig. 1.

Copyright © 2022 by author(s)

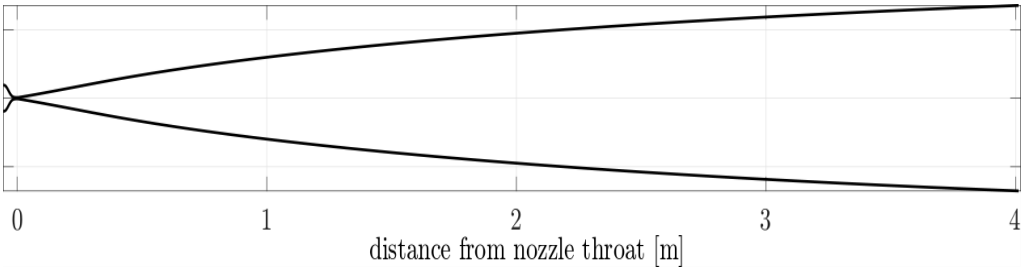

Fig 1. ***VKI Longshot contoured nozzle geometry***

The mean boundary layer profiles along the nozzle contour are determined with the DEKAF boundary layer code [8]. This ensures both an excellent accuracy on the profiles (compatible with boundary layer stability requirements) and efficient computations. To this end, DEKAF first requires reference boundary layer edge flow conditions. These are taken from the HYPNOZE code (therefore including real gas effects) along the inviscid contour. A simplified approach also considered a perfect gas assumption to establish boundary layer edge flow conditions (the flow Mach number being taken equal to the real gas computations, but the other quantities being derived from isentropic tables for given stagnation flow conditions). The resulting boundary layer edge conditions are indicated in Fig. 2 for the edge static pressure, static temperature, and flow Mach number. An isothermal boundary condition of T_w=293K was imposed as an additional boundary condition.

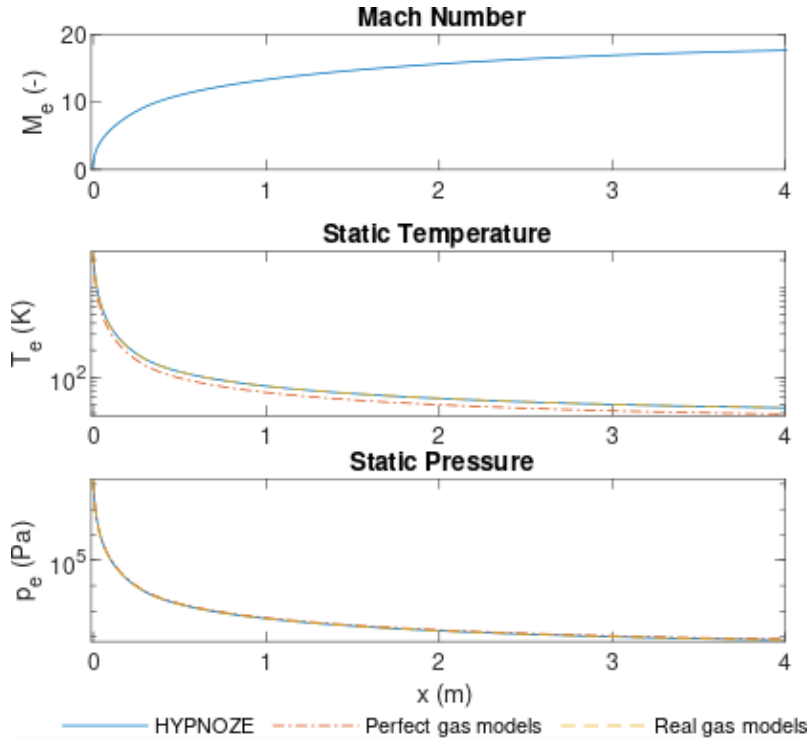

Fig 2. ***Boundary layer edge conditions***

Mean flow boundary layer profiles are generated using DEKAF by solving the boundary layer equations. Two-built-in gas models have been used: the first one with a perfect gas model, the second one with a real gas model (closer to the one available in HYPNOZE). Four different locations were considered as starting points for the marching solution of the boundary layer equations as indicated in Fig. 3: - a point at the end of the stagnation region of the nozzle (location 1), a point slightly upstream of the throat (location 2), the throat (location 3) and a point slightly downstream of the throat. HYPNOZE assumes the

Copyright © 2022 by author(s)

boundary layer is running from location 2 (i.e. the origin of the radial flow region). The thickness of the boundary layer, as measured by the total enthalpy, is relatively insensitive to that starting point, except very locally in the throat region where it is initiated (Fig. 4). Location 2 (slightly upstream of the throat) was used for the bulk of the analysis presented hereafter as it provides a smooth growth for the boundary layer and seems more physically reasonable than either of the two more downstream locations.

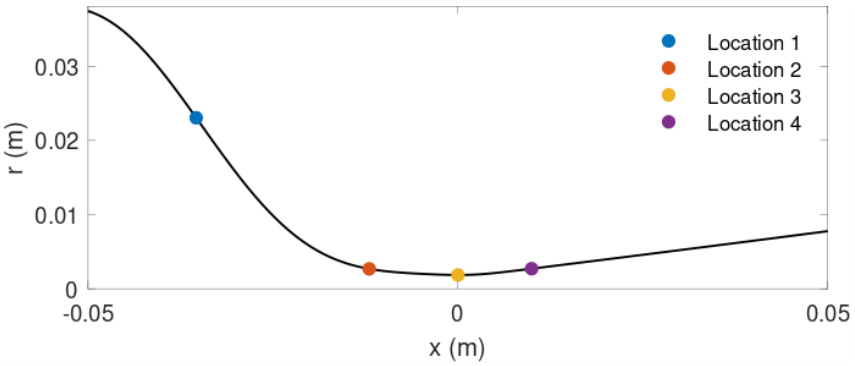

Fig 3. ***Different boundary layer starting points along the nozzle***

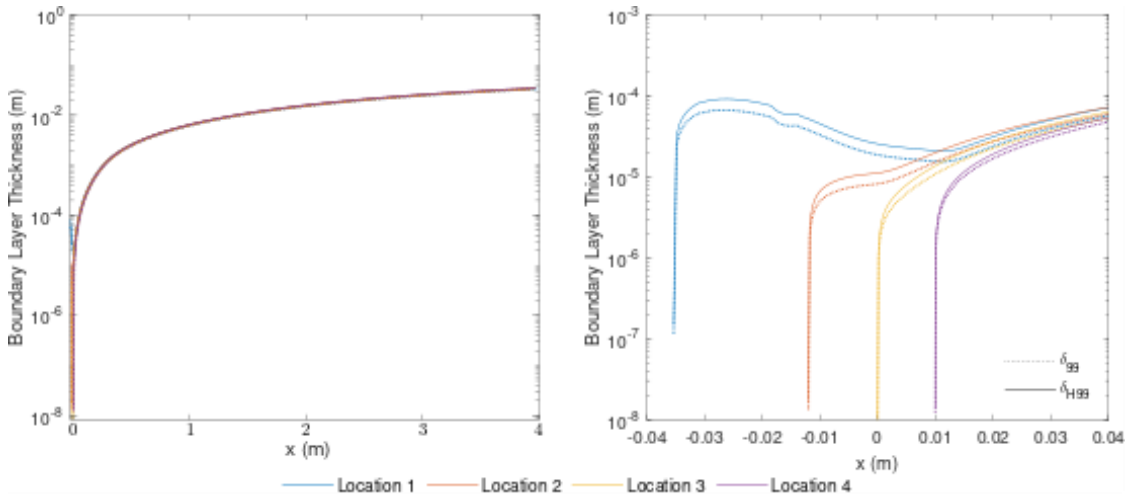

Fig 4. ***Boundary layer thickness along the nozzle for different boundary layer starting points***

DEKAF boundary layer profiles generated along the length of the Longshot tunnel are provided in Fig. 5. These profiles, taken from the nozzle locations corresponding to Mach numbers of 1, 2, 3, etc show the development of the momentum and thermal boundary layers. Both sets of gas models are included - while qualitatively similar, the set of perfect gas models appear to overestimate the freestream temperature and the wall-normal velocity gradient, particularly in the early stages of boundary layer development. Profiles are shown plotted against the self-similar wall-normal coordinate:

$$\eta = \int_0^y \frac{u_e(x,y)}{\sqrt{(2\xi(x)}} \rho(x,y) dy$$

$$\xi = \int_0^x \rho_e(x) u_e(x) \mu_e(x) dx$$

Copyright © 2022 by author(s)

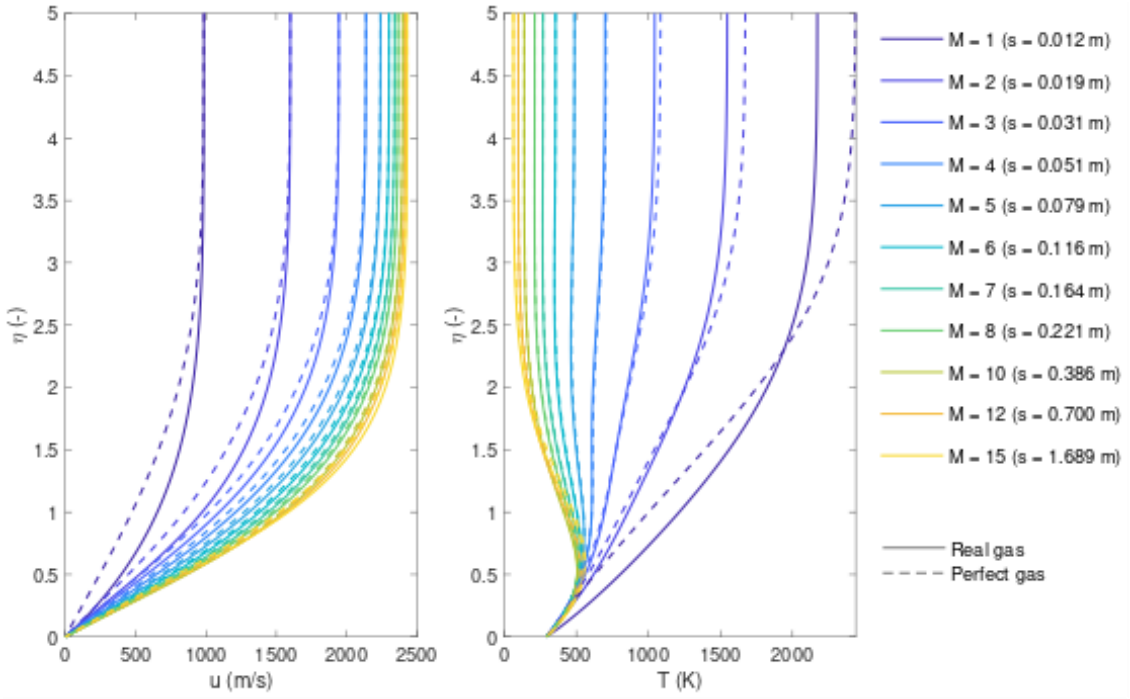

Fig 5. ***Boundary layer profiles along the nozzle***

3. Longshot nozzle boundary layer characterization

In order to characterize the boundary layer developing along the nozzle wall, Pitot pressure measurements are conducted with a rake probe at several streamwise positions indicated in Table 1. The rake consists of 30 probes with 10 mm spacing between them. Each of them is equipped with a separate piezoresistive Nova NPP-301A-100A pressure transducer, which were calibrated against a reference Ceravac CTR-100 sensor. During this campaign 22 probes (Probe Nr.1-17 and Nr.19-23) were used.

Table 1. Test matrix of the Pitot rake measurements.

Shot Nr.	**1844**	**1846**	**1847**	**1848**	**1849**
Streamwise position	20 mm	254 mm	20 mm	– 600 mm	– 875 mm
Rake alignment	Vertical	Vertical	Horizontal	Vertical	Vertical

Since these profile measurements were performed in separate shots, advection time delays must be accounted for in order to compare distributions resulting from similar reservoir conditions. Figure 6. presents the locations of the pitot rake and its individual probes with respect to the nozzle contour and compares the Pitot profiles obtained at various streamwise locations. The pressure distributions correspond to $p_0 = 166\ \mathrm{MPa}$ reservoir pressure, which is the designed operational point of this nozzle. The plotted profiles are normalized with the actual mean reservoir pressure, and the contour plot indicates the pitot pressure distribution.

Copyright © 2022 by author(s)

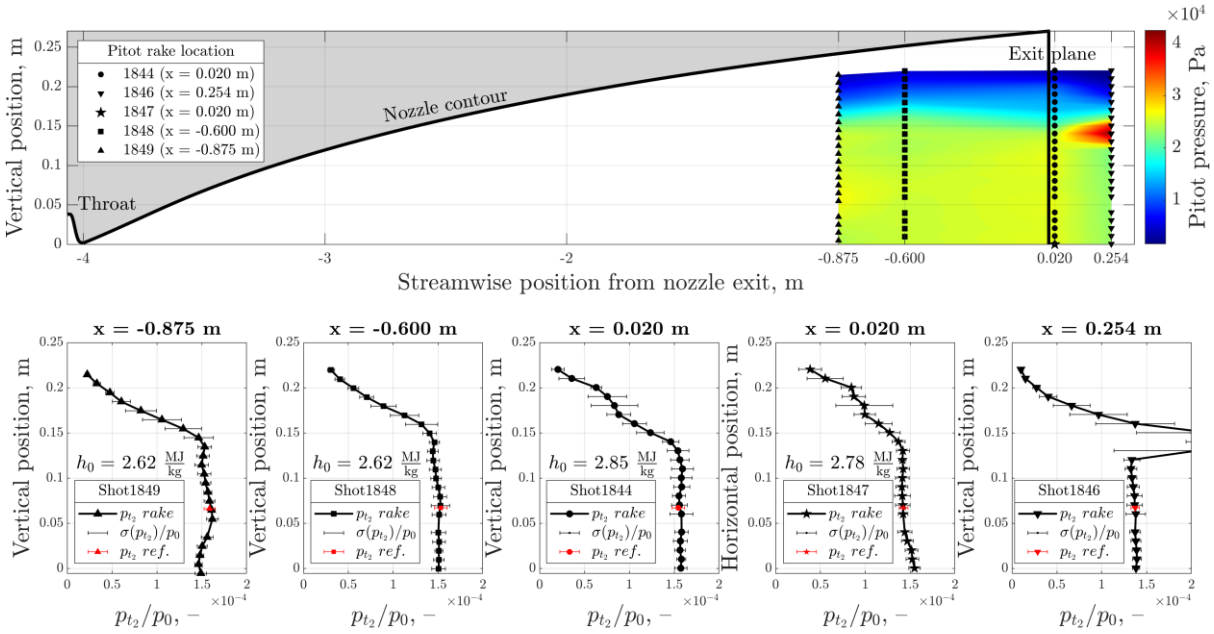

Fig 6. Normalized Pitot pressure profiles measured along the nozzle.

A window of 1 ms was used to compute the averaged pitot pressures and their standard deviation $\sigma(p_{t_2})$ which is indicated with the error bars. The red markers noted by $p_{t_2}\,ref.$ are indicating the normalized pitot pressure measured by a reference total pressure probe. The nose-tip of this probe was located at the same streamwise location as the rake, between probe Nr.20 and Nr.21, 65.5 mm to the left of the rake's plane. Revolving its radial distance measured from the nozzle axis, into the plane of the rake, a good match can be observed in the normalized pitot pressures.

The vertical and the horizontal profiles at 20 mm downstream of the nozzle exit, show a fair match at the centerline of the nozzle, but they are slightly asymmetrical. Apart from the most upstream measurement, the vertical pitot profiles are generally flat up to half nozzle radius (measured from the centerline), which indicates a good uniformity in the core flow. The horizontal profile measured at 20 mm has a small peak close to the centerline, while the one at -875 mm upstream shows a saddle-like behavior. The pitot pressure profile measured at $x = 254\ \mathrm{mm}$ exhibits a large pressure peak in the vicinity of the boundary layer edge. This is associated with oblique shock waves induced by the overexpanded nature of the hypersonic nozzle flow for this operating condition at this particular time instant. For subsequent time instants, the oblique shock waves would gradually travel further upstream as a result of the decreasing static pressure within the hypersonic jet (following the reservoir pressure decay) in combination with the increasing pressure within the test chamber (due to the continuous amount of gas being discharged in there). As expected in hypersonic nozzles, a thick boundary layer is present along the wall. Starting from the vicinity of the wall and moving towards the core flow, one can observe that the standard deviation, i.e., the fluctuation of the pitot pressure, is significantly increasing since the probes are exposed to the turbulent fluctuations of the viscous layer. Within the core flow, the standard deviation decreases.

The evolution of normalized pitot pressure profiles are presented in Fig. 7 as the reservoir pressure decays between $p_0 = 210 - 110\ \mathrm{MPa}$. The lines are colored from red to blue depending on the reservoir pressure they correspond to. In the top right plot, the temporal variation of the reservoir pressure during each run is presented. The selected reference time instant $t = 0\ \mathrm{ms}$ refers to the instant for which the reservoir stagnation pressure reaches half of its peak amplitude. This 100 MPa pressure sweep corresponds to an approximately 18 ms time frame. The dotted lines present p_0 measurements where the oscillations are induced by the cavity-line system present in front of the sensor. The continuous curves correspond to exponential fits. Time instances when the reservoir pressure is reaching a specific value were identified based on the smoothed curves, and the mean pressures were computed based on the original signals. Similarly, to the plot in Fig. 6, a time window of $\Delta t = 1\ \mathrm{ms}$ was used for the computation of the mean pitot pressures and the corresponding mean reservoir pressures.

Copyright © 2022 by author(s)

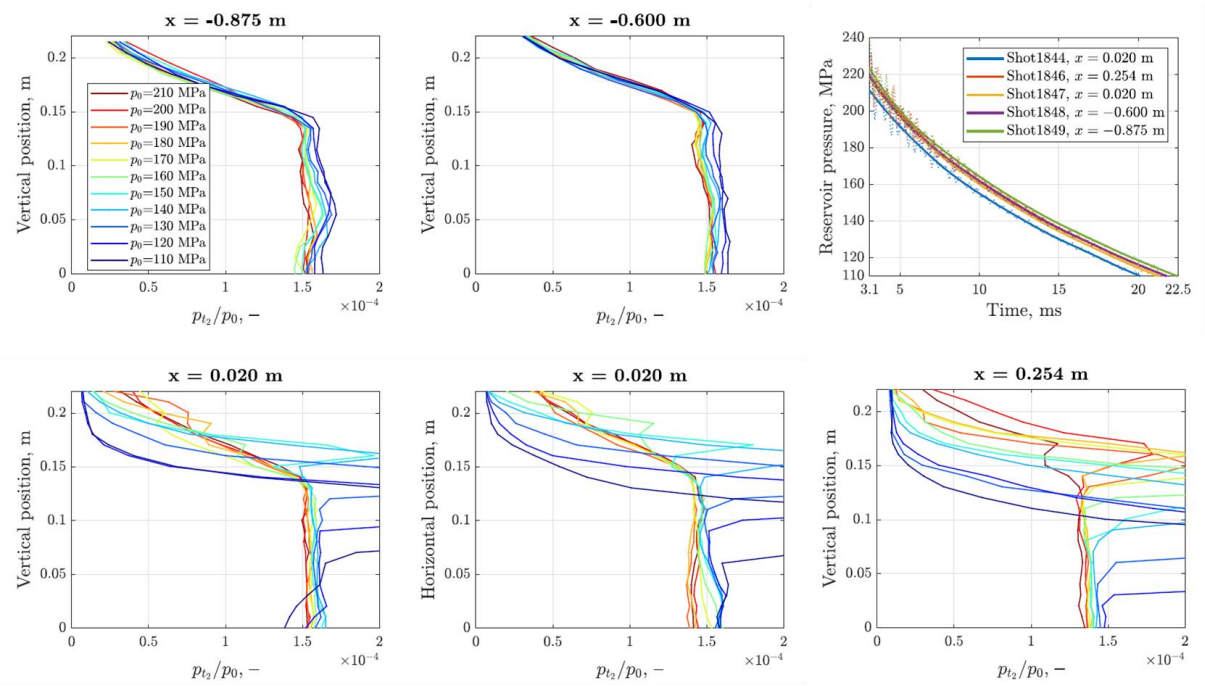

Fig 7. Normalized Pitot pressure profiles corresponding to various reservoir conditions.

At $x = -875$ mm, the pitot profiles at higher reservoir pressures show a good uniformity in the core of the flow and a slightly increasing and then decreasing trend at the edge of the boundary layer. As the pressure is decreasing the profile becomes more and more undulating. A valley of lower pitot pressures is forming close to the centerline and the peak point is moving away from the nozzle axis to approximately 55 mm. The profiles measured at $x = -600$ mm are showing a similar behavior as the most upstream ones as the reservoir conditions decay. They remain more homogeneous within the core flow. One can observe that the fluctuations inside the boundary layer are moderate with respect to the profiles measured at other locations. At this axial location, all the profiles seem to commonly have an inflection point around 180 mm. The vertical profile at $x = 20$ mm downstream of the nozzle exit presents a very good uniformity inside the core flow until 130 MPa. The horizontal profile has a small peak at the edge of the core, already at high reservoir pressures. The two profiles are showing a fair agreement inside the boundary layer, but they are asymmetric close to the centerline. It is important to note that the horizontal and vertical profiles were not measured during the same experiment.

Attempts were made to synchronize the data by accounting for advection time delays and evaluate the profiles at equal reservoir pressures, but the total enthalpies may still differ. Moreover, this computation is relying on the flow velocity resulting from the full freestream rebuilding, hence it is also dependent on the enthalpy of the flow. It is visible on both profiles that already at 150 MPa, a peak starts to grow and move from the boundary layer towards the core. Below 130 MPa reservoir pressure, an oblique shock wave induced by the overexpanded structure of the jet is present. It gradually moves upstream the nozzle and is responsible for the larger pressures measured near the edge of the boundary layer and gradually moving towards the nozzle center line. At the most downstream test location, firmly constant normalized profiles were found in the core flow, similarly to the vertical profile measurement close to the nozzle exit. The process of the jet closure is well visible on the profiles of this streamwise position, and as it can be expected when moving further away from the nozzle exit, the rapid evolution of the profiles indicate limited useful test times.

As a final remark, the typical thickness of the boundary layer as well as the fluctuations level reported from the pitot pressure measurements, near the wall, indicate clearly the turbulent regime of the nozzle wall boundary layer, as it has been already pointed out in earlier studies [9].

Copyright © 2022 by author(s)

4. Longshot boundary layer stability investigation

4.1. Linear Stability Theory

The boundary layer profiles obtained with DEKAF were used to solve the equations of linear stability theory using the VESTA toolkit [10] [11]. This allowed the calculation of real and imaginary components of the complex streamwise wavenumber α for selected values of frequency ω and spanwise wavenumber β at effectively any point in the Longshot nozzle domain. In practice, analyses were primarily limited on the development of second mode instabilities for which $\beta = 0$. A convergence study was conducted to evaluate the sensitivity of the solution to the number of points placed in the boundary layer by the stability code. Convergence appears to be reached with 200 points in the boundary layer. This profile resolution was then adopted for all subsequent calculations.

A series of frequency sweeps were carried out in which the amplification rate, $-\alpha_i$, was calculated across a span of instability frequencies $f = \omega/2\pi$ by tracking a preselected eigenvalue corresponding to the second mode disturbance eigenvector. These curves are shown in Figure 8. The amplification rate curves show a wide range of frequencies and instability magnitudes. At early stages of the nozzle, there is a wide band of unstable instabilities at very high frequencies (for example, the peak at M = 3 occurs at approximately 50 MHz); this frequency band narrows further downstream, and the implification rates decrease significantly.

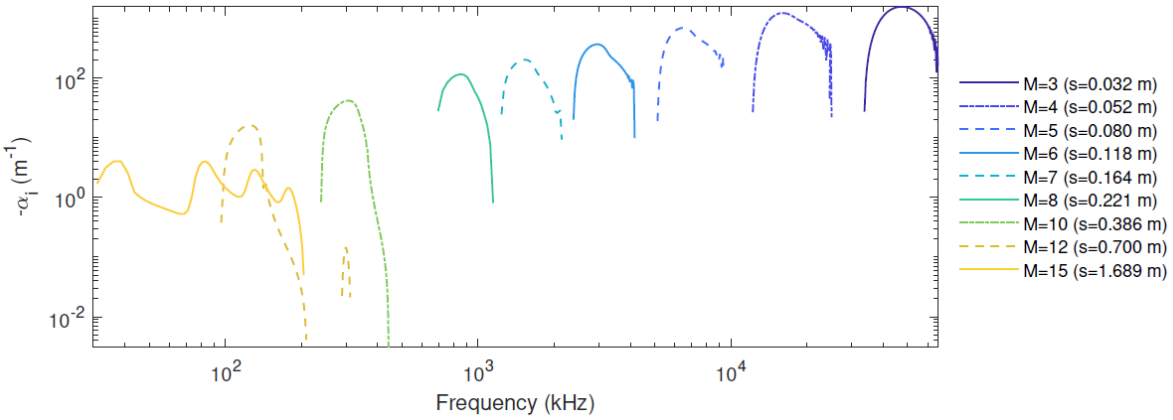

Fig 8. Amplification rates of second-mode instabilities with respect to frequency

The amplification rate curves are more clearly visible when plot on linear axis as shown in figure 9 for some specific Mach numbers.

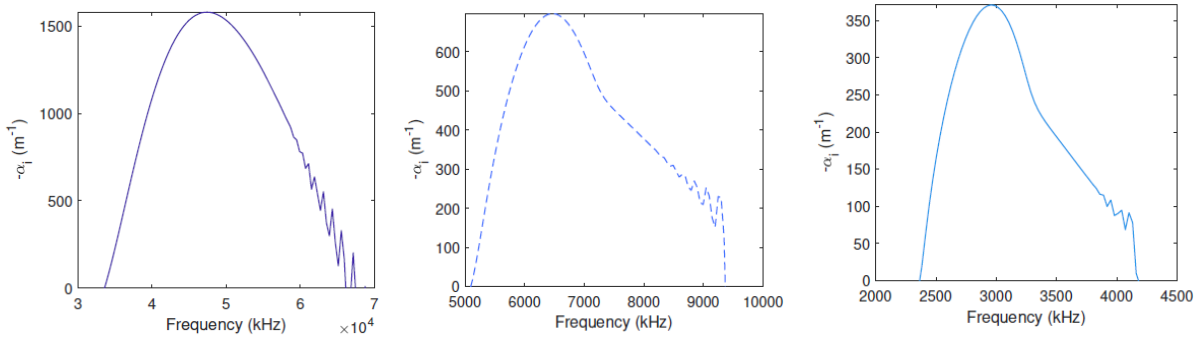

M=3 (x = 0:032 m) M=5 (x = 0:080 m) M=6 (x = 0:118 m)

Fig 9. Amplification rates of second-mode frequencies for some individual Mach numbers

The same narrowing of the band of unstable frequencies is apparent; in addition, higher instability modes begin to appear above Mach 10. In the Mach 4-8 range, the curves show significant unstable supersonic second mode waves, evidenced by the change in slope which occurs after the peak for these curves (for example, at around 7.2 MHz at M = 5 and 3.2 MHz for M = 6) [12]. These supersonic modes radiate into the freestream, meaning that they could be a source of acoustic disturbances in the Longshot nozzle and test section [13]. It is also possible that the Dirichlet boundary conditions imposed in this work are

Copyright © 2022 by author(s)

artificially restricting the development of these modes [14]. The jagged shape on the descending side of some curves (particularly at lower Mach numbers) appears to be an artefact of the Chebyshev collocation method.

In order to characterize the range of unstable frequencies in the near-throat region, the neutral curve was obtained [15]. Figure 10 shows a relatively broad band of unstable frequencies near the throat (considering the logarithmic scale in the vertical axis), that narrows drastically as the flow progresses downstream. The multiple modes shown in the higher-Mach frequency sweeps would appear downstream of the shown neutral curve, which has been truncated due to the difficulties posed by this behavior.

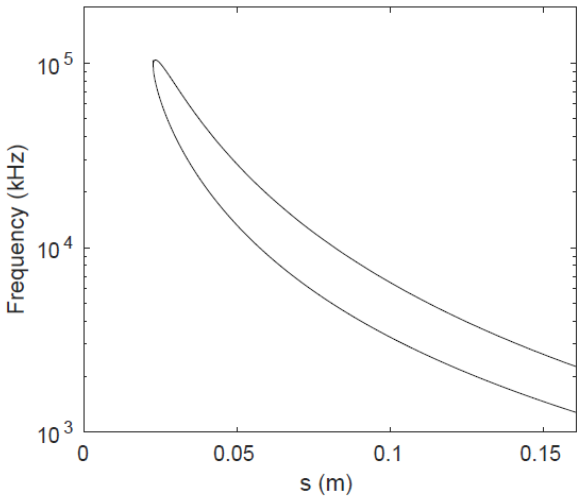

Fig 10. Neutral curve for the Longshot nozzle wall boundary layer flow

The VESTA toolkit was also used to calculate N factors, i.e. the logarithms of the integrated values of the normalized growth rates as pioneered by van Ingen [16]. The N factor provides an idea of how much a particular instability has grown; transition onset is assumed when it reaches an empirically-determined value. A plot of N factors corresponding to a broad range of frequencies is shown in Figure 11.

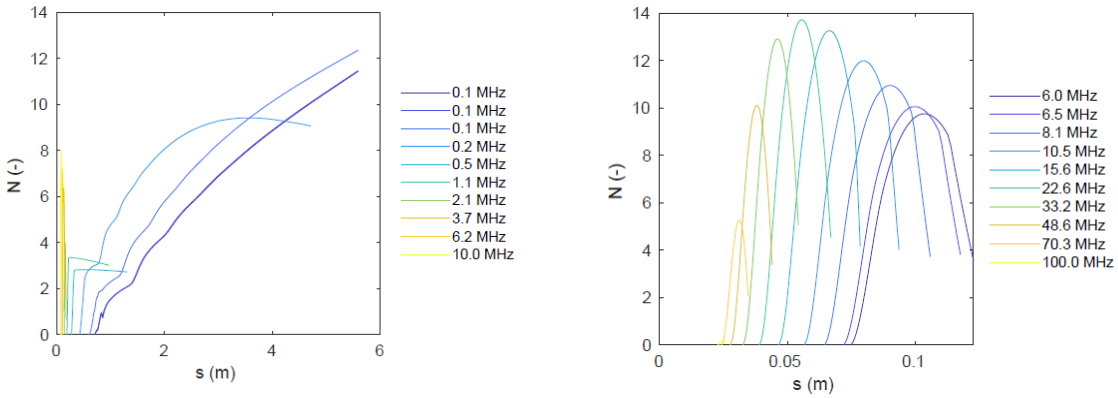

(Along the entire nozzle domain) (Near-throat region)

Fig 11. N factor curves for the Longshot nozzle

A more detailed examination of the N factor curves shows two families of high N factor curves: one near the throat and one far downstream in the nozzle. However, the slow-growing, low-frequency instabilities which dominate in the downstream region only become critical long after the boundary layer is expected to transition to turbulence. Therefore, it is the upstream region in the vicinity of the nozzle throat which appears to be most relevant to transition. A second set of N factor curves corresponding to the throat region of the nozzle is provided in the same Figure (Fig. 11); these show growth of the high-frequency second mode and likely transition onset before s = 5 cm as the value of the N factor is exceeding 7-8.

Copyright © 2022 by author(s)

4.2. Wall roughness considerations

Given the surface finish of the Longshot nozzle, which has an RMS roughness of 0.4 μm, measured in the region of the nozzle throat, it is likely that distributed roughness plays a significant role in the development of boundary layer instabilities and subsequent transition to turbulence. To evaluate this possibility, the roughness height Reynolds number, Re_k, was calculated using the reported RMS roughness value; it is shown plotted as a function of downstream distance in Figure 12.

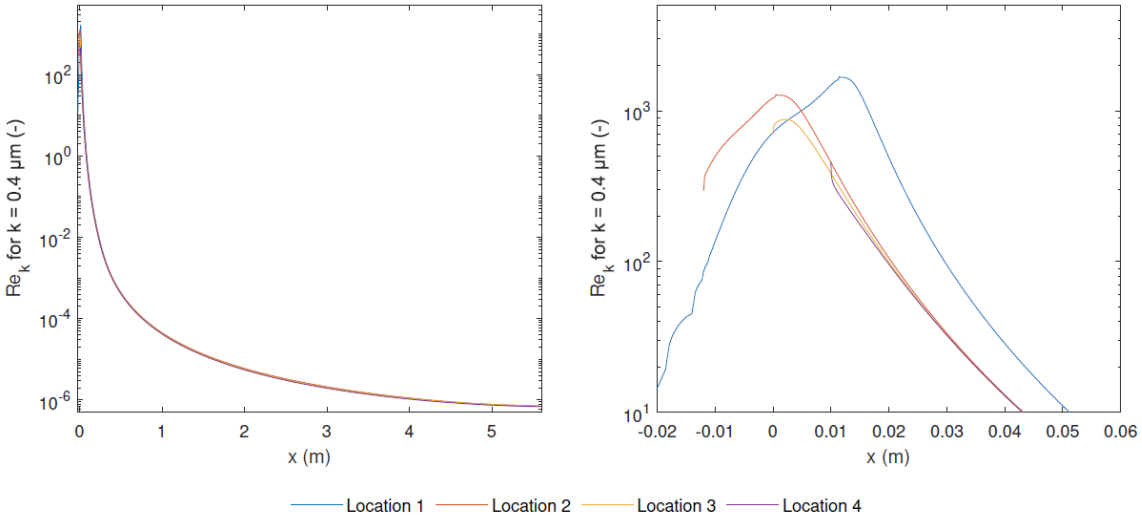

Fig 12. Roughness height Reynolds number (Rek) vs. surface distance coordinate in the Longshot nozzle (left) and in the throat of the Longshot nozzle (right)

The peak roughness height Reynolds number is roughly 1000 for all boundary layer start locations (most significantly, the two upstream of the throat), which is well above values typically used to predict roughness-induced transition in high-speed wind tunnels. A 2008 review by Schneider [17] found values ranging from Re_k = 25 to as low as 12 used as design parameters to ensure roughness-independent transition. One could note that the consideration of real gas effects has some noticeable impact on the value of Re_k; when compare with the calculations made with the perfect gas model. The inclusion of real gas effects appears to lower the peak roughness Reynolds number slightly [18].
It is worth emphasizing that these calculations use the RMS value of roughness, whereas most literature calculates Re_k using the maximum peak-to-valley height. This value has not been measured for the Longshot nozzle, but by definition it must be higher than the reported RMS roughness height of 0.4 μm, so the values of Re_k reported here are conservative. To reduce the effect of wall roughness to the point of insignificance would require the throat of the Longshot nozzle to be polished to a maximum roughness height (i.e. the maximum height above the mean surface) of 59 Å to reach Re_k = 25 or 29 Å to reach Re_k = 12. How close or far this is from the current configuration of the Longshot nozzle remains unknown without a more detailed understanding of the nozzle surface.

5. Conclusions

A basic analysis of the boundary layer in the VKI Longshot tunnel has been performed using linear stability theory. Using freestream conditions calculated using the method of characteristics, solutions to the boundary layer equations have been obtained and used to solve the equations of linear stability theory. Measurements of Pitot pressure profiles have been presented that indicate the development of a turbulent boundary layer along the nozzle wall. To investigate the laminar to turbulent transition a preliminary analysis has been conducted using Linear Stability Theory method.

Stability calculations illustrate the behavior of the most significant instability modes in the nozzle. These calculations show that second mode instabilities slightly downstream of the throat dominate - due to the thin boundary layer, this mode exists in a very high frequency band which narrows and moves to lower

Copyright © 2022 by author(s)

frequencies in the downstream region. In any case, eN theory suggests that transition should occur quite early in the nozzle - N factors as high as 14 were obtained around 5 cm downstream of the throat. Depending on the freestream disturbance levels, this could potentially trigger transition at a very early streamwise location.
Given that the inclusion of real gas effects significantly altered the shape and height of the boundary layer profiles, inclusion of these effects in the stability theory calculations would also be worthwhile, as they are likely to alter the predicted growth of second-mode waves. Applying different boundary conditions to the freestream would also be worth investigating as the current Dirichlet condition may be overly restrictive to the development of supersonic instability modes. Further investigation of other instability mechanisms is necessary to fully characterize the stability of the boundary layer on the Longshot nozzle wall | given the low Mach numbers at which maximum N factors were reached, it is possible that first-mode waves are a dominant mechanism; further downstream, Görtler waves should also be explored since they are associated with streamwise concavity.
Considering the wall surface, it could suggest that transition in the Longshot tunnel is likely driven by the distributed roughness in the throat; the nominal surface finish roughness of 0.4 μm seems to be significantly above the level which would be required to maintain undisturbed laminar ow; in fact, it seems possible that the roughness is significant enough to induce a bypass transition mechanism. To maintain a freestream ow which is unaffected by the presence of distributed surface roughness, the analysis performed in this work suggests that a surface finish of approximately 29-59 Å is required. Further study of the throat region, including detailed measurements of the surface condition and advanced CFD in this critical region could help elucidate the true effect of distributed roughness on boundary layer development.

The analyses of the boundary layer in the Longshot tunnel suggest that ow is likely to be fully turbulent for most of the length of the nozzle, and indeed quite possibly its entire effective length. It is probable that roughness in the throat leads directly to transition; if it does not, then linear growth of instabilities can be expected to cause transition within a few centimeters of the throat. Further study of the throat surface, the disturbance levels existing upstream of the throat, and the behavior of instability modes other than the second mode could shed more light on the specific physical phenomena which lead to transition in the Longshot tunnel.

References

[1] M. V. Morkovin, E. Reshotko and T. Herbert, "Transition in open flow systems - a reassessment," *Bulletin of the American Physical Society,* p. 39(9):1882, 1994.

[2] A. V. Fedorov, "Transition and stability of high speed boundary layers," *Annual Review of Fluid Mechanics,* pp. 43(1):79-95, 2011.

[3] N. Sandham, E. Schülein, A. Wagner, S. Willems and J. and Steelant, "Transitional Shock-Wave/Boundary-Layer Interactions in Hypersonic Flow," *Journal of Fluid Mechanics,* pp. 752 (6), pp. 349-382, 2014.

[4] G. Grossir and B. Dias, "Flow characterization of the VKI Longshot wind tunnel," in *VKI Lecture Series 2018/19.*, von Karman Institute for Fluid Dynamics, 2018.

[5] G. Grossir and Z. Illich, "Numerical modeling of the VKI Longshot compression process," in *VKI Lecture Series 2018/19*, von Karman Institute for Fluid Dynamics,, 2018.

[6] R. Span, E. W. Lemmon, R. T. Jacobsen, W. Wagner and A. Yokozeki, "A reference equation of state for the thermodynamic properties of nitrogen for temperatures from 63.151 to 1000K and pressures to 2200MPa," *Journal of Physical and Chemical Reference Data,* vol. 29, pp. 1361-1433, 2000.

[7] G. Grossir and O. Chazot, "Design of axisymmetric contoured nozzles for calorically and thermally imperfect gases using the Hypnoze code," in *HiSST: 2nd International Conference on High-Speed Vehicle Science & Technology*, Bruges, Belgium, 2022.

Copyright © 2022 by author(s)

[8] K. J. Groot, F. Miró Miró, E. S. Beyak, A. J. Moyes, F. Pinna and H. L. Reed, "DEKAF: Spectral multi-regime basic-state solver for boundary-layer stability (AIAA 2018-3380)," in *2018 Fluid Dynamics Conference AIAA*, 2018.

[9] G. Grossir, Hypersonic Wind Tunnel Flow Characterization and application to Boundary Layer Stability Investigations, PhD Thesis, ULB - Von Karman Institute, 2014.

[10] F. Pinna, Numerical Study of Stability of Flows from Low to High Mach number, PhD thesis, ULB - Von Karman Institute, 2012.

[11] F. Pinna, "Vesta Toolkit: A Software to Compute Transition and Stability of Boundary Layers," AIAA paper 2013-2616, 2013.

[12] N. Bitter and J. Shepherd, "Stability of highly cooled hypervelocity boundary layers," *Journal of Fluid Mechanics,* vol. 778, pp. 586-620, 2015.

[13] P. V. Chuvakhov and A. V. Fedorov, "Spontaneous radiation of sound by instability of a highly cooled hypersonic boundary layer," *Journal of Fluid Mechanics,* vol. 805, pp. 188-206, 2016.

[14] L. Zanus, F. Miro Miro and F. Pinna, "Parabolized stability analysis of chemically reacting boundary-layer," *Part G: Journal of Aerospace Engineering,* vol. 1, no. 234, pp. 79-95, 2020.

[15] F. Miro Miro, Numerical Investigation of Hypersonic Boundary-Layer Stability and Transition in the presence of Ablation Phenomena, PhD Thesis, ULB - Von karman Institute, 2020.

[16] J. van Ingen, "A suggested semi-empirical method for the calculation of the boundary layer transition region," Technische Hogeschool Delft, Technical Report VTH-74, 1956.

[17] S. P. Schneider, "Effects of Roughness on Hypersonic Boundary Layers Transition," *Journal of Spacecraft and Rockets,* vol. 45, no. 2, pp. 193-209, 2008.

[18] G. Andrews, "Stability of the Nozzle Wall Boundary layer in the VKI Longshot Tunnel," Von Karman Insitute, 2020.

Copyright © 2022 by author(s)